Journal of Energy Chemistry 116 (2026) 558–565

Contents lists available at ScienceDirect

Journal of Energy Chemistry

journal homepage: www.elsevier.com/locate/jechem

http://www.journals.elsevier.com/journal-of-energy-chemistry/

Electrocatalytic ammonium nitrate synthesis through integrating nitric oxide redox reactions over porphyrinic metal–organic frameworks

Yi Tan [a], Xiaokang Chen [a], Jian Yuan [a], Guan Sheng [b], Wei-Qiao Deng [a], Ghim Wei Ho [c], Hao Wu [a,d,*]

[a] Institute of Frontier Chemistry, School of Chemistry and Chemical Engineering, Shandong University, Qingdao 266237, Shandong, China
[b] Department of Applied Physics, The Hong Kong Polytechnic University, Hong Kong 999077, China
[c] Department of Electrical and Computer Engineering, National University of Singapore, Singapore 117583, Singapore
[d] Suzhou Research Institute, Shandong University, Suzhou 215123, Jiangsu, China

ARTICLE INFO

Article history:
Received 23 December 2025
Revised 12 January 2026
Accepted 14 January 2026
Available online 28 January 2026

Keywords:
Nitric oxide
Porphyrin
Metal–organic frameworks
Ammonium nitrate

ABSTRACT

The conversion of nitric oxide (NO), a gaseous pollutant with an intermediate nitrogen oxidation state, into value-added ammonium nitrate (NH_4NO_3) via redox processes offers a sustainable alternative to conventional disposal methods, which are hampered by competing pathways that yield undesirable byproducts. Herein, we decouple the synthesis of NH_4NO_3 into electrochemical NO oxidation (NOOR) and reduction (NORR) by employing H-terminated and Cu-metallated porphyrinic metal–organic framework catalysts (H-PMOF and Cu-PMOF, respectively), leveraging their tailored coordination environments and varied NO adsorption configurations. The H-PMOF favors O-atom adsorption via hydrogen bonding, whereas the Cu-PMOF strengthens N-atom adsorption through Cu—N interactions. They promote NOOR to NO_3^- and NORR to NH_4^+, respectively, achieving greater Faradaic efficiencies and yield rates compared to their respective counterparts. When integrated in one electrolyzer, they enable direct synthesis of NH_4NO_3 by generating 662.4 μmol of NO_3^- and 409.5 μmol of NH_4^+ hourly. Molecular dynamics simulations reveal differences in adsorption modes, while computational results identify the rate-determining dehydrogenation ($^*HNO_3 \rightarrow {}^*NO_3$ for NOOR) and hydrogenation steps ($^*NO \rightarrow {}^*NHO$ for NORR), with both catalysts exhibiting reduced energy barriers. This work presents a strategy for directing NO redox reactions through coordination engineering, paving the way for sustainable nitrogen valorization.

1. Introduction

Human activities, particularly those related to combustion engines, industrial operations, and agricultural activities, have elevated nitric oxide (NO) to harmful concentrations, which poses serious risks to both ecosystems and human health if not properly addressed [1–9]. Traditional techniques for NO elimination through selective catalytic reduction necessitates considerable amounts of valuable ammonia (NH_3) or hydrogen (H_2) as reducing agents, ultimately converting NO into harmless but economically unviable dinitrogen gas (N_2) [10–17]. In contrast, a more appealing approach involves transforming NO, which exists in an intermediate nitrogen valence state, into valuable nitrogen-containing products such as ammonia (NH_3) and nitrates (NO_3^-) through reduction and oxidation, respectively, along with producing cost-effective ammonium nitrate (NH_4NO_3) by integrating these redox reactions [18]. This integrated electrosynthesis method demonstrates promising economic feasibility by enabling the co-production of both NH_4^+ and NO_3^- ions from a single feedstock (NO) within one electrolyzer, thereby significantly lowering equipment and energy expenses compared to conventional NH_4NO_3 production methods [19–21], which rely on the energy-intensive and CO_2-emitting Haber-Bosch process for NH_3 synthesis and the Ostwald process for nitric acid.

Steering NO redox reactions towards the synthesis of NH_4NO_3 is chemically intricate due to the presence of competing pathways that may yield undesired byproducts such as nitrite (NO_2^-) and N_2 [22–26]. To achieve selectivity, it is essential to precisely regulate the coordination chemistry of the intermediates involved in these redox processes. Porphyrin-based complexes, characterized

* Corresponding author.
E-mail address: haowu2020@sdu.edu.cn (H. Wu).

https://doi.org/10.1016/j.jechem.2026.01.029

by their tunable redox-active centers [27,28], present a promising platform for directing both the reduction and oxidation of NO. The hydrogen (H) atom located at the center of the porphyrin ring can participate in hydrogen bonding, preferentially interacting with the oxygen (O) atom of NO (Fig. 1), thereby facilitating direct nitrogen (N) oxygenation and enhancing the NO oxidation reaction (NOOR). This claim is supported by density functional theory (DFT) calculations (Fig. S1), which indicate that the O-terminated configuration has a higher adsorption energy (−0.93 eV) than the N-terminated configuration (−0.68 eV). However, the progression of the NO reduction reaction (NORR) entails several preliminary steps preceding the N hydrogenation, including the cleavage of O—H and O—N bonds, followed by the re-adsorption of N, ultimately diminishing catalytic efficiency. Notably, the center cavity of the porphyrin ring is well-suited for metalation, leading to an $M–N_4$ configuration (where M could be Fe, Cu, etc.) [29,30]. The unpaired electron on the N atom of the NO molecule enables substantial overlap with the *d*-orbitals of transition metals (such as Cu^{2+}, which has a $3d^9$ configuration), modifying the adsorption characteristics of NO through the formation of strong M–N bonds. The alternating adsorption of NO is evidenced by an increased adsorption energy of −1.22 eV (Fig. S1) for the N-terminated configuration, as opposed to −1.01 eV for the O-terminated configuration, which necessitates only the cleavage of the N—O bond prior to hydrogenation on N, thereby enhancing the catalytic efficiency of NORR.

In this context, we propose to fine-tune the activities of NOOR and NORR by altering the coordination environment of the porphyrin center for the electrocatalytic synthesis of NH_4NO_3 from NO. As a proof-of-concept, we developed two catalysts, H-terminated and Cu-metallated porphyrinic metal–organic frameworks (H-PMOF and Cu-PMOF, respectively), which demonstrated promising performance for generating NO_3^- via NOOR and NH_4^+ via NORR, respectively. The H-PMOF achieved a Faradaic efficiency (FE) of 89.0% and a yield rate of 1025.4 μmol h^{-1} mg_{cat}^{-1} for NO_3^-, while Cu-PMOF reached a FE of 90.2% and a yield rate of 382.5 μmol h^{-1} mg_{cat}^{-1} for NH_4^+, both outperforming their respective counterparts. When integrated H-PMOF and Cu-PMOF as the anode and cathode, respectively, 662.4 μmol of NO_3^- and 409.5 μmol of NH_4^+ were produced at −1.2 V within one hour. Molecular dynamics (MD) simulations revealed distinct NO adsorption configurations on H-PMOF and Cu-PMOF, highlighting O-atom adsorption on H-PMOF and a stronger preference for N-atom adsorption on Cu-PMOF. Moreover, DFT calculations identified the rate-determining steps: the dehydrogenation process from $*HNO_3$ to $*NO_3$ for NOOR (exhibiting a lower energy barrier on H-PMOF) and the hydrogenation step from *NO to *NHO for NORR (showing a reduced energy barrier on Cu-PMOF). This work demonstrates a decouple-and-integrate strategy that separately optimizes NO oxidation and reduction using tailored PMOFs, then combines them in a single electrolyzer for direct NH_4NO_3 production—a route that aligns with sustainable nitrogen valorization.

2. Experimental

2.1. Materials

V_2AlC (ChemicalBook, 99.99%), tetrakis (4-carboxyphenyl) porphyrin (TCPP, CHEMSOON, 99.99%), copper-tetrakis (4-carboxyphenyl) porphyrin (Cu-TCPP, CHEMSOON, 99.99%), tetramethylammonium hydroxide (TMAOH, Aladdin, 99%), hydrogen fluoride (HF, AR), N, N-dimethyl formamide (DMF, AR), ethanol (AR), and methanol (AR) were all purchased from Sinopharm Chemical Reagent Co., Ltd. Deionized (DI) water was used in all experiments.

2.2. Synthesis of V_2CT_x MXene

1 g of V_2AlC was added slowly into a 50 mL plastic bottle with 20 mL of HF. The mixture was stirred at 37 °C for 24 h. Then, the mixture was centrifuged at 5000 r min^{-1} for several times until the pH reached about 7. Subsequently, 12 mL of deionized (DI)

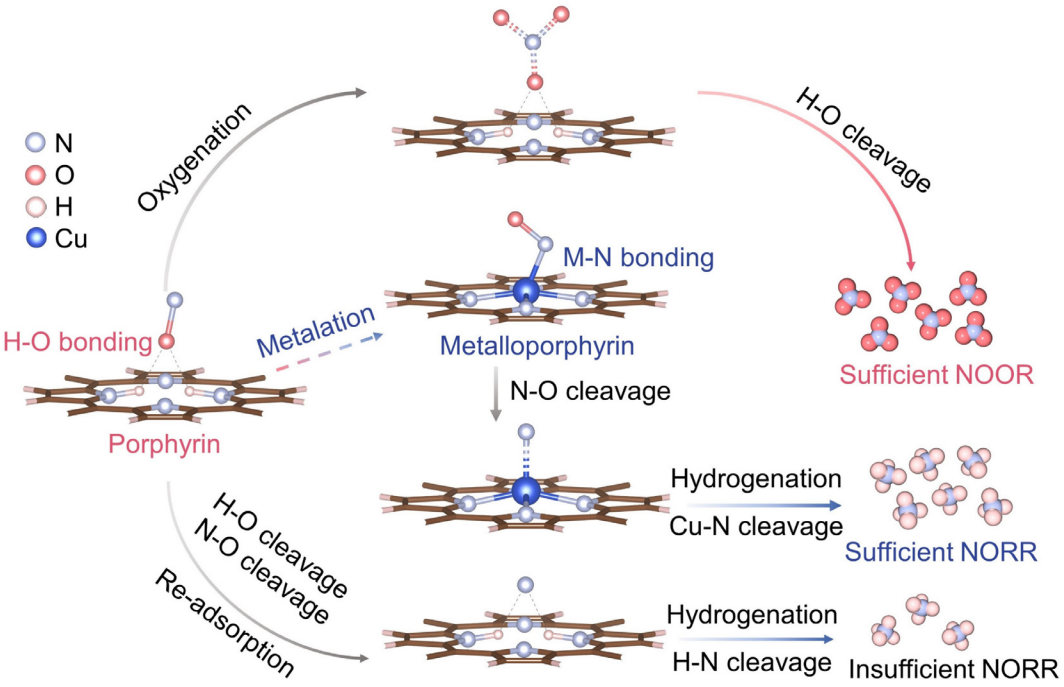

Fig. 1. Schematic diagram of directing NO redox reactions by porphyrin and metalloporphyrin. Upon interaction with metals, NO can donate its lone pair to form a coordinate bond with the metal, further promoting the formation of M–N bonds. π-back bonding from the metal *d*-orbitals into the π* orbitals of NO could enhance the stability of these M–N bonds.

H_2O and 3 mL of tetramethylammonium hydroxide (TMAOH, 1 M) were added to the as-obtained precipitate and stirred for 12 h at room temperature. Slurry was obtained by centrifugation (8000 r min^{-1}). Finally, V_2CT_x MXene dispersion, with a concentration of ~2.48 mg mL^{-1}, was obtained by collecting the supernatant at 4000 r min^{-1} for 2 min.

2.3. Synthesis of Cu-PMOF and H-PMOF

9.68 mL of V_2CT_x MXene was precipitated by centrifugation for 25 min, and then mixed with 100 mg of tetracarboxylphenyl porphyrin (TCPP) and 20 mL of dimethylformamide (DMF). Then, the mixture was transferred into a 50 mL Teflon autoclave and kept at 150 °C for 10 min. After the reaction, the mixture was centrifugally washed with DMF and methanol at 10,000 r min^{-1} for three times until the supernatant was clear. H-PMOF was obtained by vacuum drying at 80 °C. To prepare Cu-PMOF, Cu-TCPP was used while other reaction conditions being unchanged.

3. Results and discussion

3.1. Structure and characterizations of the catalysts

The H-PMOF was synthesized using a method established in previous work [31,32], incorporating V_2CT_x (T_x = terminal atom) MXene as the metal precursor and tetracarboxyphenyl porphyrin (TCPP) were employed as ligand source (refer to details in Methods). Notably, a heterostructured MOF-MXene composite was generated by partially converting the MXene into MOF, enhancing the adsorption capacity for NO. The enhanced NO adsorption on the heterostructure may also be facilitated by the surface-terminated functional groups of MXene (e.g., –OH, –O), which can weakly interact with NO molecules, thereby increasing the local NO concentration and promoting subsequent redox reactions. Herein, to facilitate redox reactions of NO molecules at the three-phase interface, this heterostructured catalyst was selected. Similarly, a Cu-PMOF composite was synthesized using Cu-metalated TCPP as the ligand. The two catalysts are referred to as H-PMOF and Cu-PMOF, respectively, for simplicity. X-ray diffraction (XRD) analysis confirmed the successful synthesis of both heterostructured samples, displaying characteristic peaks for both MXene and PMOFs (Fig. S2). The (002) diffraction peak of MXene exhibited a shift to lower angles in both samples compared to pristine MXene, attributable to increased interlayer spacing upon the incorporation of PMOFs. Scanning electron microscopy (SEM) and transmission electron microscopy (TEM) images revealed a lamellar structure for both samples (Figs. S3 and S4). High-resolution TEM (HRTEM) imaging under low-dose conditions (detailed in the Supporting Information) was conducted to elucidate their fine structures [33]. The HRTEM images depicted mixed periodic hexagonal and cubic frameworks (Fig. S5), indicative of the MXene and PMOF characteristics, respectively. These findings confirm the coexistence of MXene and MOF components. A representative HRTEM image of H-PMOF under defocused conditions displays ordered square cages (Fig. 2a), where bright dots signify the V nodes. In Cu-PMOF, regularly arranged dots of lower brightness were detected at the centers of the cages, corresponding to Cu atom coordination within the porphyrin centers (Fig. 2b). These geometries align with the projected structural models (Fig. 2c), reinforcing the incorporation of Cu in Cu-PMOF.

Fourier transform infrared (FT-IR) spectroscopy indentified significant peaks at 968 and 1000 cm^{-1} for H-PMOF and Cu-PMOF (Fig. 2d), correlating with the in-plane vibrations of N—H and Cu—N bonds, respectively [29]. UV–visible absorption spectra indicated a reduction in Q-band numbers for Cu-PMOF compared to H-PMOF (Fig. S6), implying the generation of higher D_{4h} symmetric inner nitrogen atoms in the porphyrin macrocycle [34,35]. These observations confirm the formation of the Cu–N_4 configuration in Cu-PMOF. Additionally, the composition and chemical states of the two samples were assessed using X-ray photoelectron spectroscopy (XPS). The N 1*s* spectra revealed that C—NH and C═N—C bonds predominated in H-PMOF (Fig. 2e), with C═N—C bonds diminishing while the Cu—N became dominant, further verifying the coordination between Cu and N. Characteristic peaks in the XPS Cu 2*p* spectra incdicated that Cu in Cu-PMOF predominantly exists in the 2+ valence state (Figs. S7 and S8). Energy-dispersive X-ray spectroscopy (EDX) mapping results demonstrated a uniform distribution of C, N, O, and V in PMOF and Cu-PMOF (Figs. S9 and S10). The inductively coupled plasma optical emission spectrometer revealed mass proportions of Cu and V in Cu-PMOF to be 3.24% and 30.62%, respectively, resulting in an estimated atomic ratio of Cu to MXene of approximately 1:5 in the composite. Moreover, NO temperature-programmed desorption profiles indicated that both samples exhibited two distinct peaks at approximately 125–150 °C and 180–235 °C (Fig. 2f), corresponding to physical and chemical adsorption of NO, respectively. Cu-PMOF exhibited intensified NO adsorption peaks, indicating greater NO adsorption capacities, while H-PMOF demonstrated stronger chemical adsorption capabilities [36]. Elevated temperatures (above 280 °C) leads to the decomposition of PMOFs (Fig. S11).

3.2. Electrochemical NOOR and NORR performance

The electrochemical performance of NOOR was assessed in NO-flowed environment (2% NO in 98% Ar) using 0.1 M Na_2SO_4 electrolytes within a conventional three-electrode setup (see detailed procedures in the Supporting Information). The linear sweep voltammetry (LSV) profiles showed a marked increase in current densities in the presence of NO at potentials exceeding 1.3 V vs. reversible hydrogen electrode (RHE) for both catalysts (Fig. 3a), suggesting the occurrence of NOOR. H-PMOF demonstrated higher current densities than Cu-PMOF at potentials greater than 1.6 V vs RHE, indicating its superior catalytic activity towards NOOR. The primary products of NOOR, NO_3^- and NO_2^-, were quantified using colorimetric methods (Figs. S12 and S13). The quantitative values match with the results obtained through ion chromatography for both NO_2^- and NO_3^- (Figs. S14 and S15), confirming the methodological reliability. Across the whole potentials ranging from 1.4 to 1.8 V, H-PMOF exhibited higher FEs and yield rates of NO_3^- than those for Cu-PMOF (Fig. 3b; Figs. S16 and S17). In contrast, Cu-PMOF exhibited greater FEs and yield rates for NO_2^-. At 1.8 V, H-PMOF achieved a maximum $FE_{NO_3^-}$ of 89.0% and yield rate of 1025.4 μmol h^{-1} mg_{cat}^{-1}, outperforming Cu-PMOF, which recorded 47.1% and 640.0 μmol h^{-1} mg_{cat}^{-1}, respectively. Consequently, H-PMOF is favored as a catalyst for NO_3^- synthesis via NOOR. H-PMOF exhibits NOOR performance that renders it highly competitive with other reported catalysts (Table S1). Additionally, H-PMOF exhibited stable FEs and yield rates for NO_3^- across 10 consecutive measurement cycles (Figs. S18 and S19) and retained characteristic peaks of the H-PMOF component in post-test XRD and sheet-like morphology in SEM analyses (Fig. S20), demonstrating its remarkable stability as an electrocatalyst for NOOR.

In contrast to NOOR, the ammonia synthesis via NORR on H-PMOF involves more complex processes, which appear to be more feasible with Cu-PMOF. To explore this hypothesis, electrocatalytic performance tests for NOOR were conducted on both catalysts using the same electrolytic cell and electrolyte as previously described. The LSV results revealed increased current densities for both catalysts in the presence of NO at potentials ranging from

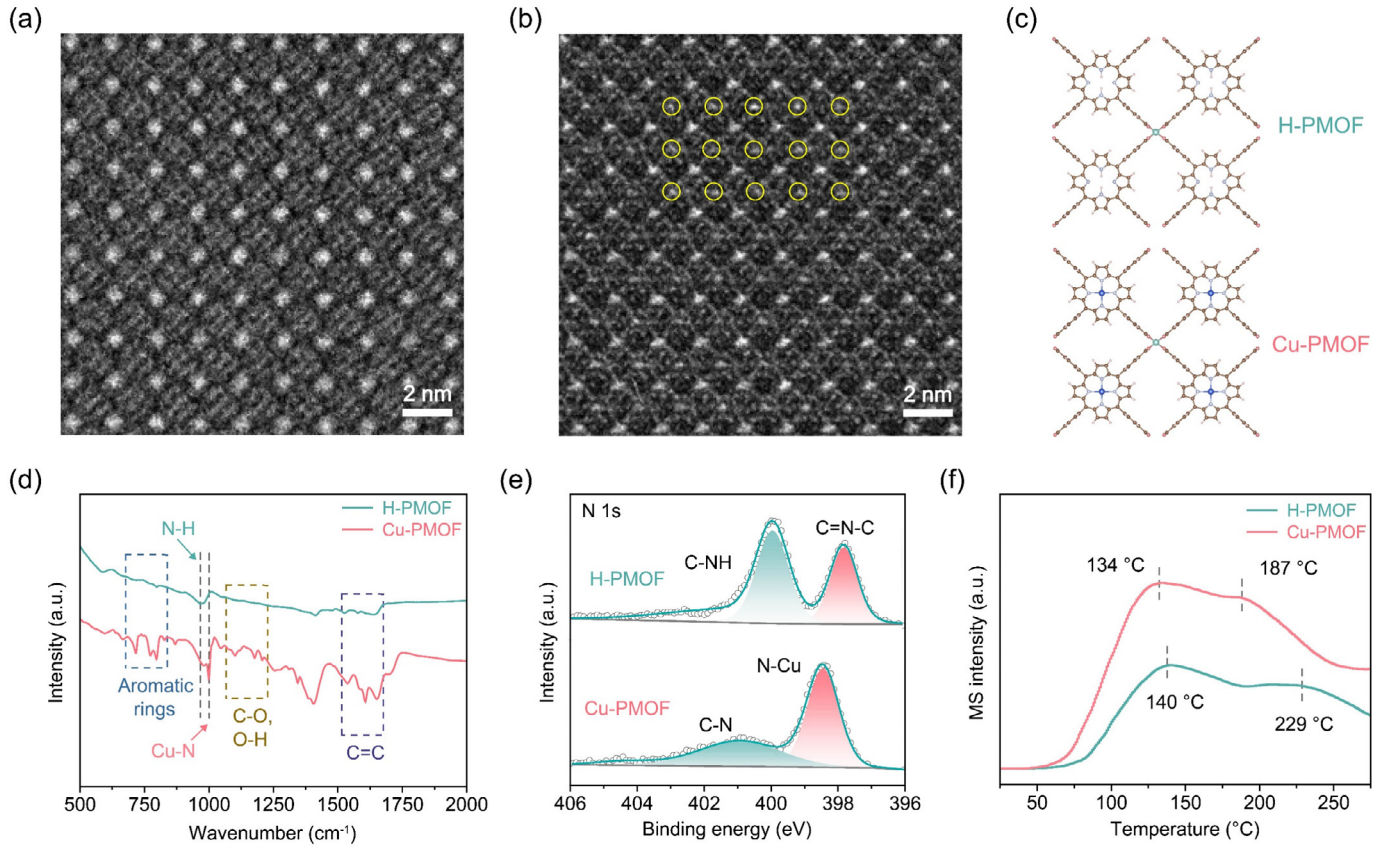

Fig. 2. Low-dose HRTEM images of (a) H-PMOF, and (b) Cu-PMOF. (c) Structural models, (d) FT-IR spectra, (e) XPS N 1*s* spectra, and (f) NO temperature-programmed desorption profiles of H-PMOF and Cu-PMOF, respectively.

0 to –1.0 V for (Fig. 3c), indicating the occurrence of NORR. The current density for H-PMOF significantly declined after –0.9 V, while that of Cu-PMOF remained relatively stable, suggesting that NO might hinder the hydrogen evolution reaction of H-PMOF, indicating greater NORR catalytic activity for Cu-PMOF. The FEs and yield rates of NH_4^+ and potential reduction byproducts (N_2H_4 and NH_2-OH) for both catalysts were quantified using colorimetric techniques (Figs. S21–S23), wtih H_2 detection performed via gas chromatography. As illustrated in Fig. 3(d), Cu-PMOF exhibited higher $FE_{NH_4^+}$ values than H-PMOF from –0.9 to –1.3 V, achieving a maximum $FE_{NH_4^+}$ of 90.2% at –1.2 V. Notably, Cu-PMOF consistently outperformed H-PMOF in NH_4^+ yield rates across all potentials due to more competitive H_2 production for the latter (Figs. S24 and S25). The maximum yield rate for Cu-PMOF reached 382.5 μmol h^{-1} mg_{cat}^{-1} at –1.3 V, nearly double that of H-PMOF, indicating superior activity for NORR. Moreover, neither catalyst produced N_2H_4 and NH_2OH during the NORR. These values of Cu-PMOF compete with the previously reported electrocatalysts for the NOOR (Table S2). Additionally, electrochemical impedance spectroscopy analyses indicate that the charge transfer resistance at the catalyst/electrolyte interface is lower for Cu-PMOF than for H-PMOF (Fig. S26), agreeing with the increased adsorption energy of NO for Cu-PMOF.

To mitigate external interference with the quantitative results, control experiments were conducted using NO-saturated electrolytes at open circuit potential, Ar-saturated electrolytes, and bare carbon paper, all of which detected negligible NH_4^+ levels (Fig. S27). Moreover, nuclear magnetic resonance (NMR) combined with isotopic labeling indicated that the amount of NH_4^+ closely matched with the values obtained through chromogenic methods (Figs. S28 and S29), confirming the reliability of the detection approach. Isotope labeling using ^{15}NO detected only $^{15}NH_4^+$ in the product, verifying that NH_4^+ originates from the NORR. Additionally, the FEs and yield rates of Cu-PMOF remained nearly steady over 10 cycles (Figs. S30 and S31). The potentials and FEs were slightly deteriorated following 40-hour consecutive galvanostatic tests (Fig. S32), with maintained characteristic diffraction peaks and plate morphology of Cu-PMOF species (Fig. S33), indicating its robust stability for electrocatalytic NORR. To elucidate the role of the Cu site in Cu-PMOF for NORR, ethylenediaminetetraacetic acid (EDTA) was utilized as a poisoning agent to obstruct the Cu site. The introduction of 0.1 M EDTA into the electrolyte led to a significant reduction in current densities for NORR (Fig. S34), alongside a nearly 50% decrease in the yield rate of NH_4^+ (Fig. S35), confirming that Cu acts as the active site for NORR. Notably, MXene displayed minimal catalytic activity for both NOOR and NORR (Fig. S36), suggesting that H-PMOF and Cu-PMOF are the primary catalytic sites.

3.3. Integrated NO redox reactions for NH_4NO_3 synthesis

The successful manipulation of NO redox reactions by tailored PMOFs motivated us to integrate these two catalysts for the direct synthesis of value-added NH_4NO_3. As depicted in Fig. 3e, H-PMOF and Cu-PMOF were integrated into a single electrolyzer, serving as the anode and cathode, respectively, with a continuous flow of 2% NO during the reaction. The integrated system yielded 662.4 μmol of NO_3^- and 409.5 μmol of NH_4^+ at –1.2 V within one hour (Fig. 3f), resulting in a molar ratio of NO_3^--to-NH_4^+ of 1.62, which closely approximates the theoretical stoichiometric ratio of 1.67, indicating that both products likely stem from NO conver-

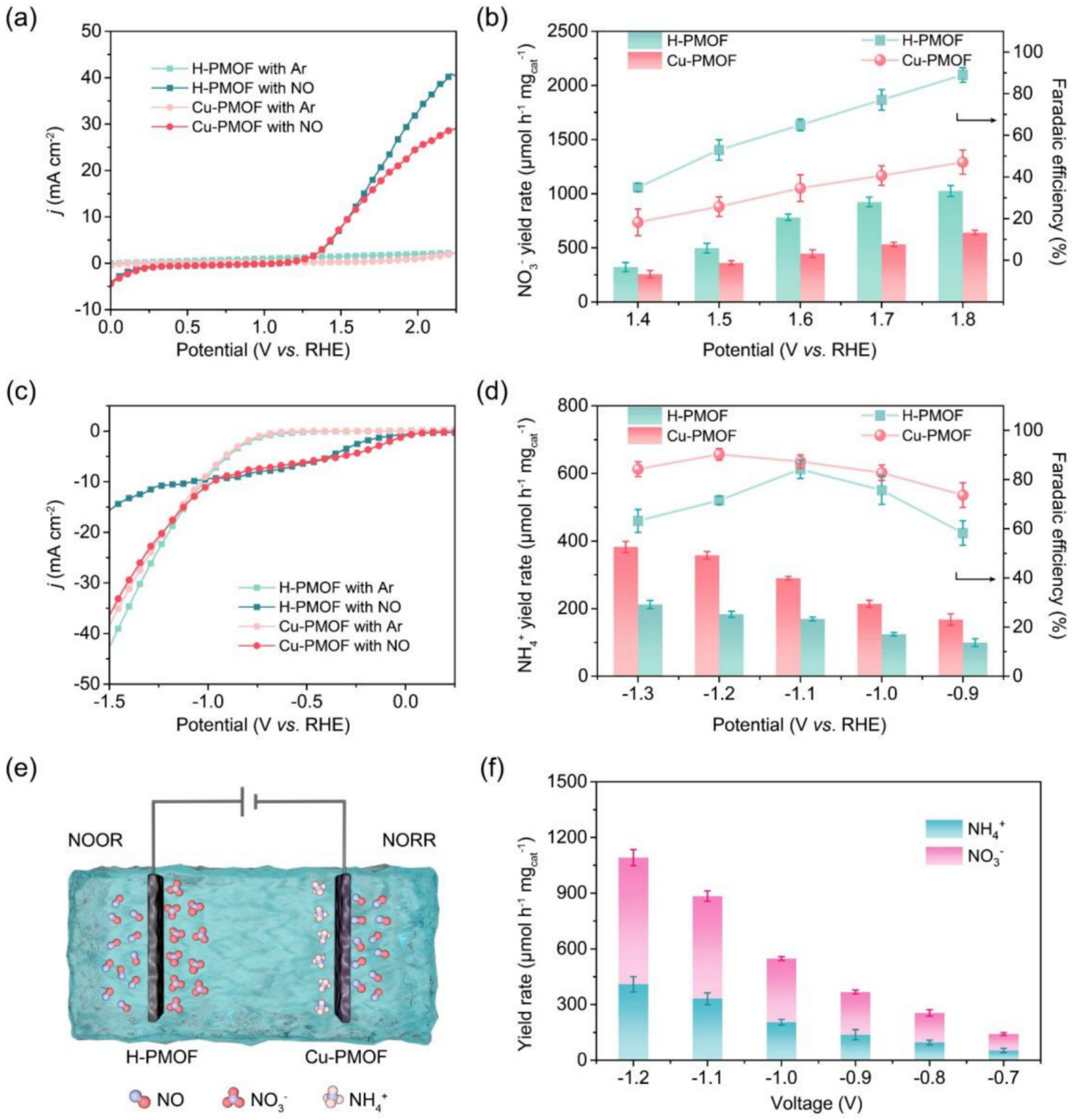

Fig. 3. (a) LSV profiles of NOOR. (b) $FE_{NO_3^-}$ and yield rates of H-PMOF and Cu-PMOF. (c) LSV profiles of NORR. (d) $FE_{NH_4^+}$ and yield rates of H-PMOF and Cu-PMOF. (e) Schematic of integrating NOOR and NORR, using H-PMOF and Cu-PMOF as anode and cathode, respectively. (f) Yield rates of NH_4^+ and NO_3^- in the integrated cell.

sion. The pH of the electrolyte exhibited a slight decrease due to the generation of additional protons throughout the overall reaction (Table S3). Even though, the current density remained relatively stable over a 12-hour stability test, suggesting its potential application as an integrated electrolytic cell for continous and long-term production of NH_4NO_3 (Fig. S37). On the other hand, in a single electrolytic cell, the NO_3^- generated at the anode could diffuse to the cathode and undergo reduction again, while the NH_4^+ product could be oxidized at the anode, resulting in decreased NH_4NO_3 yield. Therefore, we conducted a control experiment introducing stoichiometric amounts of NO_3^- and NH_4^+ ions (5:3) into the electrolytic cell for degradation testing in Ar-fed solutions. The results indicated that their concentrations remained nearly constant over a 1-hour degradation assessment (Fig. S38), confirming that negligible ions would be consumed again during NH_4NO_3 synthesis. These findings corroborate the viability of NH_4NO_3 synthesis through the integration of NO redox reactions utilizing PMOF-based electrocatalysts. Additionally, both H-PMOF and Cu-PMOF demonstrated significantly enhanced FEs and yield rates in a flow-cell configuration (Fig. S39), successfully producing white powders when employing 0.1 M ammonia as the feed electrolyte (Fig. S40). It is noteworthy that NH_4NO_3 powder is highly hygroscopic, which can lead to an overestimation of mass. Fourier transform infrared spectroscopy (FTIR) analysis of the powder revealed characteristic peaks consistent with those of NH_4NO_3 (NH_4^+ at 1600–1650, and 3000–3300 cm^{-1}; NO_3^- at 825, 1260–1520, and 1762 cm^{-1}), thereby confirming that the obtained powder is indeed NH_4NO_3 (NH_4^+: 0.1203 g, NO_3^-: 0.4453 g) and demonstrating the practical potential of the integrated device for NH_4NO_3 synthesis.

3.4. Integrated NO redox reactions for NH_4NO_3 synthesis

To elucidate the mechanism by which Cu metalation influences the NO redox reaction, we identified the relevant intermediate species using in situ electrochemical attenuated total reflection infrared spectroscopy (ATR-IR) and online differential electrochemical mass spectrometry (DEMS). In the NOOR process occurring on H-PMOF, the distinct absorbance peak at 1253 cm^{-1} corresponds to the N—O stretching vibration of $*NO_2$ (Fig. 4a), while the more pronounced peak at 1380 cm^{-1} is associated with the stretching vibration of $*NO_3$ [31]. The intensity of the $*NO_3$ peak intensified with the increase of the applied potential, aligning with experimental observations. As for the NORR on Cu-PMOF, the peaks located at around 1286 cm^{-1} and 1435 cm^{-1} are linked to the bending modes of NH_x and $*NH_2$ intermediate [4,15,36], respectively (Fig. 4b). Both peaks became more prominent with increasing negative potentials. Notably, at relatively low negative potentials (−0.9 to −1.1 V), a peak corresponding to H_2O at 1595 cm^{-1} was observed, which diminished at higher potentials (−1.2 and −1.3 V), likely due to reduced competition from hydrogen evolution. Furthermore, the *HNO peak at 1539 cm^{-1} emerged at −1.2 V, coinciding with the maximum FE, indicating the formation of the *HNO intermediate during NORR. Additionally, DEMS analysis revealed distinct signals for m/z = 62, 63, and 46 on H-PMOF during NOOR, corresponding to NO_3, HNO_3, and NO_2, respectively (Fig. 4c). The concurrent increase of the m/z = 63 signal (assigned as $^{15}NO_3^-$) fed with ^{15}NO in DEMS confirms NO as the source of NO_3^- (Fig. S41). In contrast, signals for m/z = 17, 16, and 31, corresponding to NH_3, NH_2, and HNO, respectively, were detected for Cu-PMOF during NORR (Fig. 4d). Notably, NH_2OH was absent, aligning with the experimental findings.

MD simulations were performed to investigate the bonding structure of NO molecules at the catalyst/electrolyte interface, while DFT calculations were employed to assess the adsorption energy of NO on the surfaces of the catalysts, with slab models illustrated in Figs. S42 and S43. As depicted in Fig. 5(a), dynamic snapshots revealed an accumulation of NO around the porphyrin center of Cu-PMOF. Notably, the adsorption mechanism of NO transitioned from H—O hydrogen bonding in H-PMOF to Cu—N bonding in Cu-PMOF. Moreover, Cu-PMOF exhibited higher $g(r)$ values compared to H-PMOF (Fig. S44), indicating a greater affinity for NO. This suggests that Cu metalation not only altered the adsorption mode of NO molecules but also improved their adsorption capacity. Following this, the bonding strength and charge distribution following NO adsorption were further analyzed using DFT simulations. NO was found to adsorb on H-PMOF via hydrogen bonding, with the H···O bond lengths measuring 2.07 and 2.02 Å. In contrast, on Cu-PMOF, NO was adsorbed through a Cu—N bond with a shorter length of 1.95 Å, facilitating the potential cleavage of the N═O bond. Additionally, the charge density difference diagrams illustrated charge redistribution at the interfaces of both catalysts (Fig. S45). The planar averaged charge density difference profiles indicated electron depletion on the catalyst and electron accumulation on the NO molecule (Fig. 5b). The transferred number of free electrons was 0.53 e per site for H-PMOF, while Cu-PMOF exhibited a value of 0.75 e per site. Charge transfer predominantly occurred 1.36 Å away from the porphyrin center in PMOF,

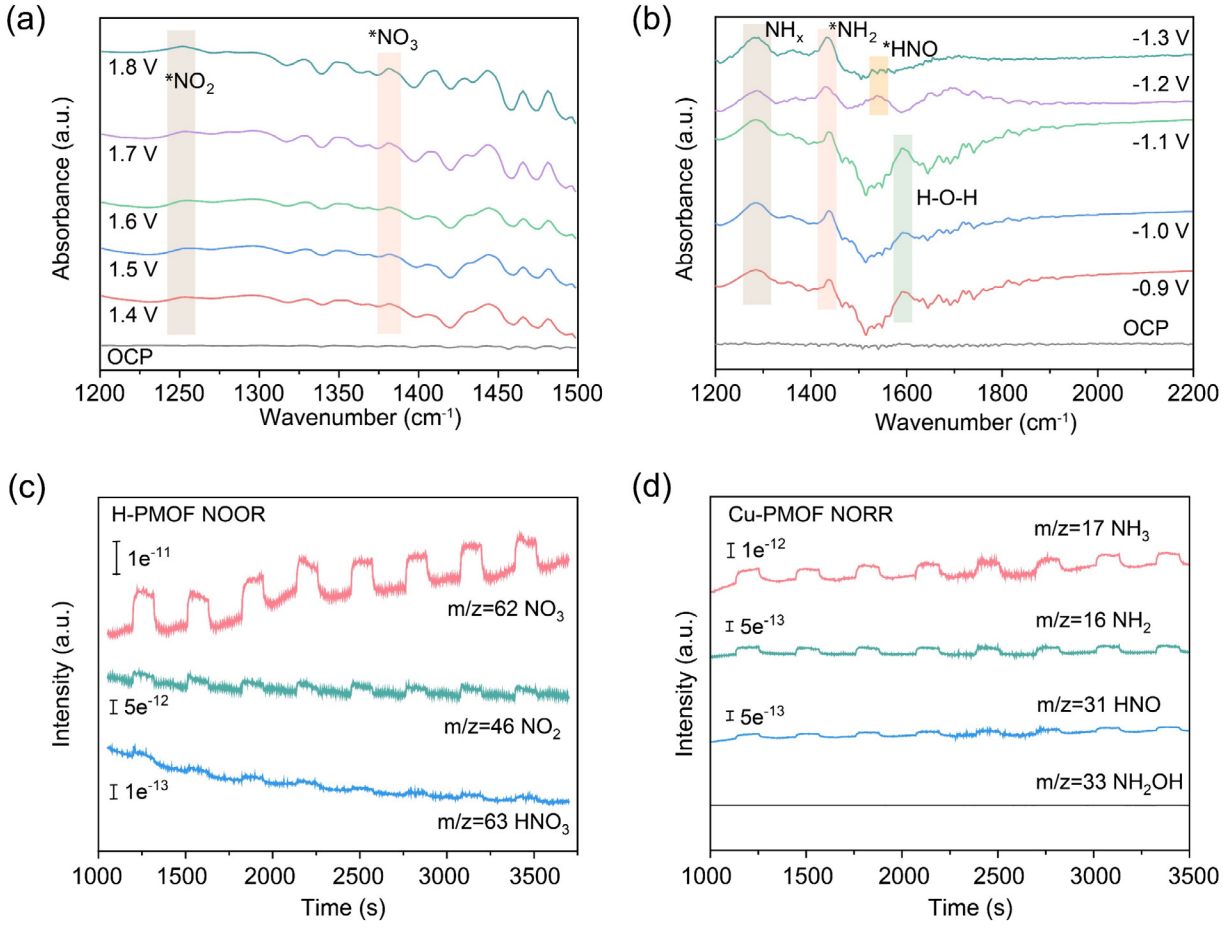

Fig. 4. In situ electrochemical ATR-IR spectra of (a) NOOR over H-PMOF and (b) NORR over Cu-PMOF. DEMS measurements of (c) NOOR over H-PMOF and (d) NORR over Cu-PMOF.

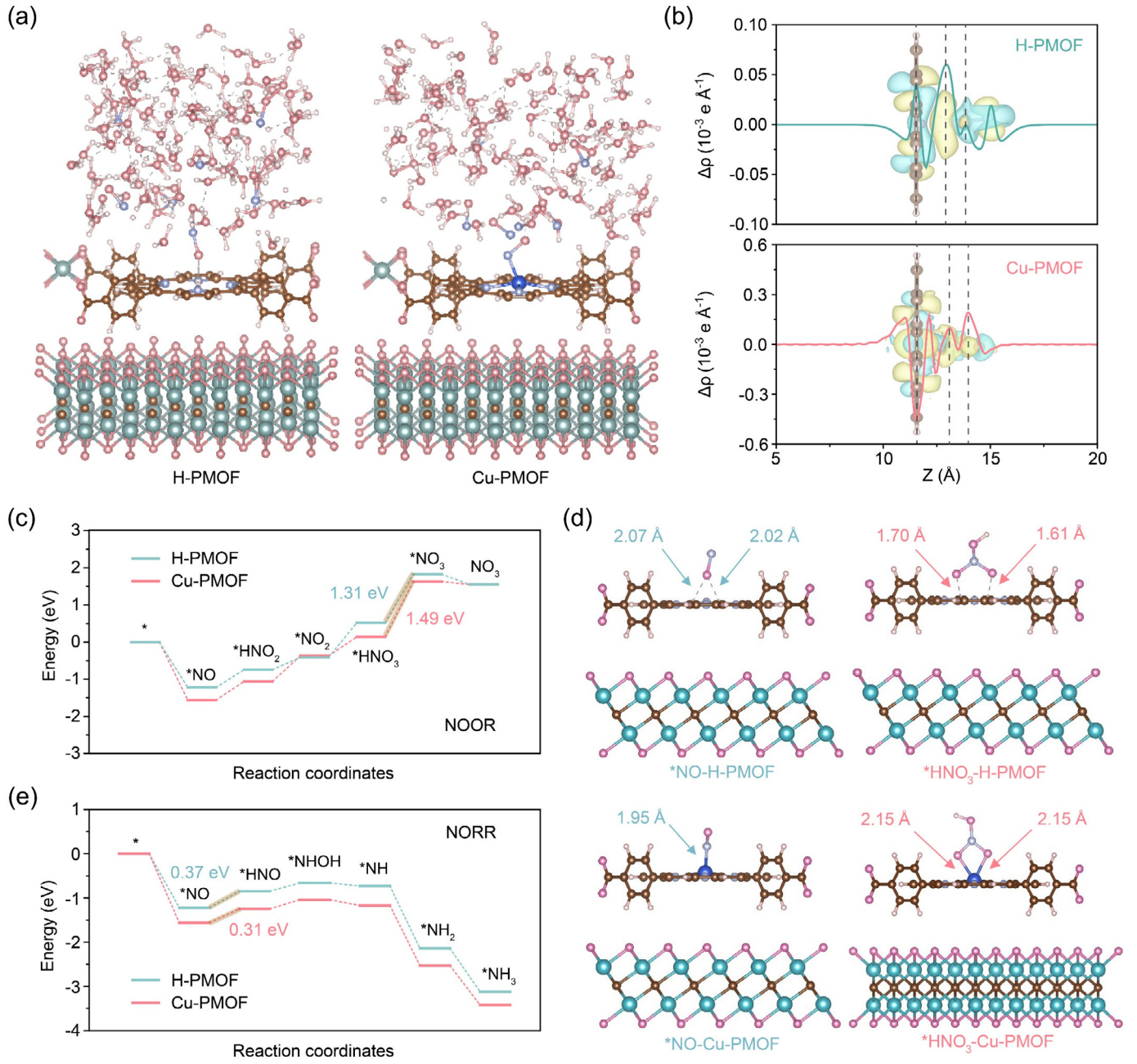

Fig. 5. (a) MD simulation of NO molecules between electrolyte and catalyst. (b) Planar averaged charge density difference profiles along the *Z* direction and charge density difference diagrams. The yellow and cyan colors denote electron accumulation and depletion, respectively. (c) Gibbs free energy diagrams of NOOR. (d) *NO-adsorbed and *HNO_3-adsorbed structural models on H-PMOF and Cu-PMOF. (e) Gibbs free energy diagrams of NORR.

with significant electron accumulation at the O atom of NO. In comparison, in Cu-PMOF, electron accumulation was observed at the N atom (1.57 and 2.50 Å from the porphyrin center), contributed by both the catalyst and the O atom of NO. This suggests that Cu metalation shifted the electron-rich site from O to N, potentially affecting the selectivity of NO redox reactions.

Accordingly, the reaction pathways were simulated using DFT calculations, where the corresponding structural models are presented in Figs. S46 and S47, while the Gibbs free energy diagrams for each step in NOOR are illustrated in Fig. 5(c). The dehydrogenation step from *HNO_3 to *NO_3 exhibited the highest reaction free energy barrier, marking the rate-determining step (RDS) for both catalysts. H-PMOF required a relatively lower RDS barrier of 1.31 eV compared to 1.49 eV for Cu-PMOF, indicating more favorable reaction kinetics. Interestingly, despite the initial differences in NO binding (*NO), the two O atoms in Cu-PMOF spontaneously coordinated with Cu following the first oxygenation step (*HNO_2), whereas they formed hydrogen bonds with two H in H-PMOF. Upon the adsorption of *HNO_3, the hydrogen bonding interaction intensified, with bond lengths decreasing to 1.70 and 1.61 Å from the initial 2.07 and 2.02 Å (Fig. 5d). In contrast, the Cu—O bond strength was comparatively weaker, characterized by a significantly longer bond length of 2.15 Å compared to the initial 1.95 Å, which may hinder the cleavage of the terminal H—O bond, i.e., the dehydrogenation step. To explain the enhanced performance of NORR on Cu-PMOF, the Gibbs free energy profiles for the entire reaction pathways were analyzed: *NO → *HNO → *HNOH → *H_2NOH → *NH_2 → *NH_3 (Fig. 5e), with opti-

mized structural models provided in Figs. S48 and S49. The RDS for both catalysts was identified as the protonation of *NO on the N site to yield *NHO. Cu-PMOF showed a lower energy barrier of 0.31 eV compared to 0.37 eV for H-PMOF, indicating improved kinetics for the NORR. This enhancement is likely attributed to electron accumulation at the N site in Cu-PMOF, facilitating the hydrogenation process.

4. Conclusions

In summary, we achieved precise control over NO redox reactions, effectively addressing selectivity issues arising from competing pathways. The metalation of the porphyrin center with Cu alters the NO adsorption mechanism from O-atom binding (via hydrogen bonding in H-PMOF) to strong N-atom coordination (through Cu—N bonding in Cu-PMOF), thereby directing the reaction pathways toward specific products. H-PMOF achieves outstanding NOOR performance, while Cu-PMOF promotes efficient NORR. The integration of these catalysts within a two-electrode electrolyzer allows for the concurrent production of NO_3^- and NH_4^+, facilitating direct synthesis of NH_4NO_3. Mechanistic investigations reveal that hydrogen bonding in H-PMOF reduces the energy barrier for $^*HNO_3 \rightarrow {}^*NO_3$ dehydrogenation during NOOR, whereas Cu—N bonding in Cu-PMOF enhances $^*NO \rightarrow {}^*NHO$ hydrogenation in NORR. These findings underscore the critical role of tailored metal coordination in influencing intermediate adsorption and reaction kinetics. This study not only advances the design of multifunctional catalysts for nitrogen cycle valorization but also establishes a viable electrochemical approach to convert NO pollutants into value-added products.

CRediT authorship contribution statement

Yi Tan: Writing – original draft, Formal analysis, Data curation, Conceptualization. **Xiaokang Chen:** Formal analysis, Data curation. **Jian Yuan:** Formal analysis. **Guan Sheng:** Formal analysis, Data curation. **Wei-Qiao Deng:** Supervision. **Ghim Wei Ho:** Supervision. **Hao Wu:** Writing – review & editing, Supervision, Formal analysis, Conceptualization.

Declaration of competing interest

The authors declare that they have no known competing financial interests or personal relationships that could have appeared to influence the work reported in this paper.

Acknowledgments

This work was supported by the National Key R&D Program of China (2022YFA1503104) and the Natural Science Foundation of Shandong Province (ZR2025MS169). This work was also Funded by Basic Research Program of Jiangsu (BK20230243) and Taishan Scholars Project (tspd20230601).

Appendix A. Supplementary material

Supplementary data to this article can be found online at https://doi.org/10.1016/j.jechem.2026.01.029.

References

[1] J. Shao, H. Jing, P. Wei, X. Fu, L. Pang, Y. Song, K. Ye, M. Li, L. Jiang, J. Ma, R. Li, R. Si, Z. Peng, G. Wang, J. Xiao, Nat. Energy 8 (2023) 1273–1283.
[2] D. Wang, Z.-W. Chen, K. Gu, C. Chen, Y. Liu, X. Wei, C.V. Singh, S. Wang, J. Am. Chem. Soc. 145 (2023) 6899–6904.
[3] P. Liao, B. Zeng, S. Li, Y. Zhang, R. Xiang, J. Kang, Q. Liu, G. Li, Angew. Chem. Int. Ed. 64 (2024) e202417130.
[4] X. Guo, T. Wu, H. Li, L. Chai, M. Liu, Angew. Chem. Int. Ed. 64 (2024) e202420346.
[5] D. Wang, X. Zhu, X. Tu, X. Zhang, C. Chen, X. Wei, Y. Li, S. Wang, Adv. Mater. 35 (2023) 2304646.
[6] W. Yang, H. Liu, X. Chang, Y. Zhang, Y. Cai, Y. Li, Y. Cui, B. Xu, L. Yu, X. Cui, D. Deng, Nat. Commun. 16 (2025) 1257.
[7] K. Chen, F. Wang, X. Lu, Y. Li, K. Chu, ACS Catal. 13 (2023) 9550–9557.
[8] D. Kim, D. Shin, J. Heo, H. Lim, J.-A. Lim, H.M. Jeong, B.-S. Kim, I. Heo, I. Oh, B. Lee, M. Sharma, H. Lim, H. Kim, Y. Kwon, ACS Energy Lett. 5 (2020) 3647–3656.
[9] S. Cheon, W. Kim, D. Kim, Y. Kwon, J.-I. Han, ACS Energy Lett. 7 (2022) 958–965.
[10] K. Chen, Y. Zhang, J. Xiang, X. Zhao, X. Li, K. Chu, ACS Energy Lett. 8 (2023) 1281–1288.
[11] L. Zhang, J. Liang, Y. Wang, T. Mou, Y. Lin, L. Yue, T. Li, Q. Liu, Y. Luo, N. Li, B. Tang, Y. Liu, S. Gao, A.A. Alshehri, X. Guo, D. Ma, X. Sun, Angew. Chem. Int. Ed. 60 (2021) 25263–25268.
[12] B. Wu, L. Huang, L. Yan, H. Gang, Y. Cao, D. Wei, H. Wang, Z. Guo, W. Zhang, Nano Lett. 23 (2023) 7120–7128.
[13] J. Long, S. Chen, Y. Zhang, C. Guo, X. Fu, D. Deng, J. Xiao, Angew. Chem. Int. Ed. 59 (2020) 9711–9718.
[14] B.H. Ko, B. Hasa, H. Shin, Y. Zhao, F. Jiao, J. Am. Chem. Soc. 144 (2022) 1258–1266.
[15] X. Guo, P. Wang, T. Wu, Z. Wang, J. Li, K. Liu, J. Fu, M. Liu, J. Wu, Z. Lin, L. Chai, Z. Bian, H. Li, M. Liu, Angew. Chem. Int. Ed. 63 (2024) e202318792.
[16] D. Wang, G. Fan, D. Luan, Y. Guo, X. Gu, X.W. Lou, Adv. Mater. 36 (2024) 2408580.
[17] J. Xian, S. Li, H. Su, P. Liao, S. Wang, Y. Zhang, W. Yang, J. Yang, Y. Sun, Y. Jia, Q. Liu, Q. Liu, G. Li, Angew. Chem. Int. Ed. 62 (2023) e202304007.
[18] S. Han, K. Yang, L. Gao, T. Li, Y. Huang, J. Zhou, B. Zhang, J. Zhu, J. Wu, B. Zhang, Y. Yu, Nat. Sustain. 8 (2025) 1068–1076.
[19] J. Xian, S. Li, H. Su, P. Liao, S. Wang, R. Xiang, Y. Zhang, Q. Liu, G. Li, Angew. Chem. Int. Ed. 62 (2023) e202306726.
[20] J. Kang, P. Liao, R. Xiang, W. Liao, C. Yang, S. Wang, Q. Liu, G. Li, Angew. Chem. Int. Ed. 64 (2025) e202419550.
[21] R. Xiang, S. Wang, P. Liao, F. Xie, J. Kang, S. Li, J. Xian, L. Guo, G. Li, Angew. Chem. Int. Ed. 62 (2023) e202312239.
[22] D. Pan, P.M. Austeria, S. Lee, H.-S. Bae, F. He, G.H. Gu, W. Choi, Nat. Commun. 15 (2024) 7243.
[23] M.D. Brown, M.H. Schoenfisch, Chem. Rev. 119 (2019) 11551–11575.
[24] Z. Hu, H.J.C.T. Wessels, T.V. Alen, M.S.M. Jetten, B. Kartal, Nat. Commun. 10 (2019) 1244.
[25] S. Zhao, J. Liu, Z. Zhang, C. Zhu, G. Shi, J. Wu, C. Yang, Q. Wang, M. Chang, K. Liu, S. Li, L. Zhang, Chem 9 (2023) 3555–3572.
[26] Y. Li, C. Cheng, S. Han, Y. Huang, X. Du, B. Zhang, Y. Yu, ACS Energy Lett. 7 (2022) 1187–1194.
[27] A. Meiller, E. Sequeira, S. Marinesco, Anal. Chem. 92 (2020) 1804–1810.
[28] Y. Tan, L. Yang, D. Zhai, L. Sun, S. Zhai, W. Zhou, X. Wang, W.Q. Deng, H. Wu, Small 18 (2022) 2204942.
[29] Y. Zhao, J. Wang, R. Pei, J. Am. Chem. Soc. 142 (2020) 10331–10336.
[30] W. Han, X. Ma, J. Wang, F. Leng, C. Xie, H.-L. Jiang, J. Am. Chem. Soc. 145 (2023) 9665–9671.
[31] Y. Tan, X. Chen, J. Yuan, G. Sheng, W.-Q. Deng, H. Wu, Angew. Chem. Int. Ed. 64 (2025) e202513441.
[32] H. Wu, M. Almalki, X. Xu, Y. Lei, F. Ming, A. Mallick, V. Roddatis, S. Lopatin, O. Shekhah, M. Eddaoudi, H.N. Alshareef, J. Am. Chem. Soc. 141 (2019) 20037–20042.
[33] L. Sun, C. Zhu, L. Li, R. Zheng, J. Yuan, Z. Li, J. Sun, G. Sheng, H. Wu, Angew. Chem. Int. Ed. 64 (2025) e202418031.
[34] Y. Wang, J. Zhang, S. Wang, Z. Tan, Y. Yang, Y. Zhao, B. Han, Q. Li, J. Xiang, ACS Catal. 14 (2024) 18397–18405.
[35] Y. Liu, Y. Wei, M. Liu, Y. Bai, X. Wang, S. Shang, C. Du, W. Gao, J. Chen, Y. Liu, Adv. Mater. 33 (2021) 2007741.
[36] J. Meng, C. Cheng, Y. Wang, Y. Yu, B. Zhang, J. Am. Chem. Soc. 146 (2024) 10044–10051.